

Characterisation of Long Baseline Calibrators at 2.3 GHz

F. Hungwe^{1,2*}, R. Ojha^{3,4}, R.S Booth^{1,2}, M.F Bietenholz^{1,5}, A. Collioud^{6,7}, P. Charlot^{6,7},
D. Boboltz⁴, A.L Fey⁴

¹ *Dept. of Physics and Electronics, Rhodes University, P.O Box 94, Grahamstown, 6140, South Africa*

² *Hartebeesthoek Radio Astronomy Observatory, P.O Box 443, Krugersdorp, 1740, South Africa*

³ *NVI, Inc., 7257D Hanover Parkway, Greenbelt, MD 20770, USA*

⁴ *United States Naval Observatory, 3450 Massachusetts Ave., NW, Washington D.C 20392, USA*

⁵ *Dept. of Physics and Astronomy, York University, Toronto, M3J 1P3, Ontario, Canada*

⁶ *Université de Bordeaux, Observatoire Aquitain des Sciences de l'Univers, BP 89, 33271 Floirac Cedex, France*

⁷ *CNRS, Laboratoire d'Astrophysique de Bordeaux-UMR 5804, BP 89, 33271 Floirac Cedex, France*

Accepted 2011 June 11. Received 2011 May 24; in original form 2010 October 29

ABSTRACT

We present a detailed multi-epoch analysis of 31 potential southern hemisphere radio calibrators that were originally observed as part of a program to maintain the International Celestial Reference Frame (ICRF). At radio wavelengths, the primary calibrators are Active Galactic Nuclei (AGN), powerful radio emitters which exist at the centre of most galaxies. These are known to vary at all wavelengths at which they have been observed. By determining the amount of radio source structure and variability of these AGN, we determine their suitability as phase calibrators for long baseline radio interferometry at 2.3 GHz. For this purpose, we have used a set of complementary metrics to classify these 31 southern sources into five categories pertaining to their suitability as VLBI calibrators. We find that all of the sources in our sample would be good interferometric calibrators and almost ninety per cent would be very good calibrators.

Key words: quasar: general - galaxies: jets - radio continuum: galaxies - techniques: interferometric

1 INTRODUCTION

High angular resolution observations of weak radio sources (where self calibration is not possible) require calibrator sources for correction of systematic effects and effects of the atmosphere on the measured visibilities. Atmospheric fluctuations cause perturbations in visibility phase which, if not corrected, seriously limit both the sensitivity and image quality of an interferometric array. Phase calibrators are also required for astrometric observations. An ideal calibrator would look the same on all observing baselines. It should be bright, unresolved, or at least compact and should not vary. A calibrator source should also be separated from the target sources by as small an angle as possible in order to look along the same line of sight through the atmosphere. Therefore, it is desirable to have calibrator sources evenly distributed across the whole sky. In practice, at radio wavelengths, calibrators are mostly Active Galactic Nuclei (AGN), whose fundamental source of power is believed to be the accretion of matter onto a super-massive black hole

(eg. Rees 1997). They are known to vary at every wavelength at which they have been studied. AGN are very compact and isotropically distributed around the sky. They are also very distant objects and therefore, generally, have no discernible proper motions on the sky. It is these qualities that make them suitable as calibrators at radio wavelengths.

Due to the limited number of radio telescopes, few surveys for calibrators have been carried out in the southern hemisphere (Ojha et al. 2004a, 2005; Fey et al. 2004a,b, 2006). Hence, there are fewer known calibrators in the south. A major expansion of radio astronomy observing capability is underway in the southern hemisphere. Two SKA (Square Kilometre Array) precursors, the South African MeerKAT (Karoo Array Telescope, Booth et al. (2009)) and ASKAP (Australian SKA Pathfinder, Johnston et al. (2008)) are presently under construction, leading to the SKA itself. It is clear that interferometry and Very Long Baseline Interferometry (VLBI) in the southern hemisphere needs a dense network of calibration sources at high resolutions and a range of frequencies. MeerKAT is the South African SKA demonstrator telescope. When completed, it will be the largest radio telescope array in the southern hemisphere. It will operate in two frequency ranges, 0.58-2.5 GHz and

* E-mail: faith@hartrao.ac.za (FH); roopesh.ojha@gmail.com (RO)

8-14.5 GHz (Booth et al. 2009). MeerKAT will participate in VLBI observations with the European VLBI Network and other VLBI arrays. The SKA will operate in the frequency range 0.7 to 25 GHz (Carilli & Rawlings 2004; Schilizzi 2007) and is expected to have much longer baselines for which a southern VLBI calibrator list will be essential.

The United States Naval Observatory, in collaboration with NASA, the Laboratoire d'Astrophysique de Bordeaux (LAB) and the National Radio Astronomy Observatory (NRAO¹) has, since 1994 been observing AGN, once every two months, through the Research and Development VLBI (RDV) experiments. This has led to a wealth of data of sources observed simultaneously at 2.3 GHz and 8.4 GHz at regular epochs. Images of these AGN form the USNO's Radio Reference Frame Image Database (RRFID) and LAB's Bordeaux VLBI Image Database (BVID)² (Fey, Clegg & Fomalont 1996; Fey & Charlot 1997, 2000; Collioud & Charlot 2009). The RRFID is a database of about 6700 images of over 700 AGN sources compiled from geodetic and astrometric VLBI experiments. The BVID contains over 1800 images of 824 radio sources. It is the goal of the ongoing RDV program to image the radio reference frame sources on a regular basis, to monitor them for variability and structural change. Piner et al. (2007) discuss jet kinematics in a subset of the RRFID sources, concentrating on the 8.4 GHz observations. Their survey is made up of RRFID sources that have been observed at 3 or more epochs from July 1994 to December 1998.

In this paper, we focus on 2.3 GHz observations of a sample of 31 potential southern VLBI calibrators (with declinations between 0 and -60°) from the kinematic survey of Piner et al. (2007). The choice of 2.3 GHz was made because both MeerKAT and ASKAP will be operating at frequencies close to this. We seek to characterise this selection of southern radio sources, and determine their suitability as calibrators for southern VLBI experiments, especially those using MeerKAT and the SKA when completed.

In the following sections, we will describe the observations and data reduction process. We will then describe the imaging and modelfitting process and go on to analyse the data and discuss the results.

2 OBSERVATIONS AND DATA REDUCTION

Research and Development VLBI (RDV) experiments are carried out using the 10 antennas of the NRAO's VLBA and up to 10 other antennas across the globe, including Hartebeesthoek (South Africa) when available. The use of the global array greatly improves the u - v coverage. Hartebeesthoek greatly improves the u - v coverage for sources in the south, which make up the sample in this paper.

The 31 southern sources included in our sample are listed in Table 1 along with their optical properties. The

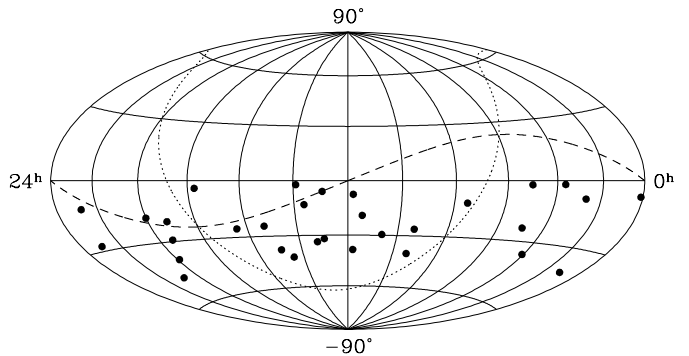


Figure 1. Sky distribution of the southern sources plotted on an Aitoff equal-area projection of the celestial sphere. The dotted line represents the Galactic plane while the dashed line is the ecliptic.

source sky distribution is shown in Figure 1. The RDV observing epochs are from July 1994 to January 2008, giving a total of 32 epochs and an average of 20 epochs per source. About 100 sources were observed in each 24 hr observing run, with an average on-source time of 15 minutes. The on-source time is not continuous, but divided into scans of between 1 and several minutes long, spaced in time to give optimal u - v coverage.

Observations were made in a dual frequency bandwidth synthesis mode to facilitate delay measurements for astrometry. Observations in this mode also allow imaging at both frequency bands. Eight individual frequency bands (IFs) were recorded simultaneously, each 8 MHz wide, with 4 at 2.3 GHz and 4 at 8.4 GHz for a total of 32 MHz in each frequency band.

The data were correlated with the VLBA correlator at the Array Operations Center in Socorro, New Mexico. The correlated data were calibrated and corrected for time and frequency dependent phase variations using NRAO's Astronomical Imaging Processing System (AIPS, Greisen (1998)). Initial amplitude calibration for each IF was accomplished using system temperature measurements and gain curves generated during observations. Fringe-fitting was done in AIPS using a solution interval equal to the scan duration and a point source model.

Amplitude calibration was improved in a second stage by using observations of sources whose core flux density is known to be ≥ 90 per cent of the total flux density. For a precise definition of the core, refer to Section 3.1. To this end, a single amplitude gain correction factor was derived for each antenna based on fitting a Gaussian model to the core component. Gain correction factors were then calculated based on the difference between the observed and the model visibilities. Finally, the amplitude gain correction factors were applied to the target sources. This is a non-standard procedure that improves the overall amplitude calibration. The accuracy of the amplitude calibration determined in this way is conservatively estimated to be within 20 per cent.

Data imaging and modelfitting were done using the Caltech Difference Mapping program 'Difmap' (Shepherd, Pearson & Taylor 1995), after inspecting the data and editing out obvious bad points. The data were im-

¹ The National Radio Astronomy Observatory is a facility of the National Science Foundation operated under cooperative agreement by Associated Universities, Inc

² The web site for the RRFID is located at <http://rorf.usno.navy.mil/rrfid.shtml> and the BVID at <http://www.obs.u-bordeaux1.fr/BVID/>

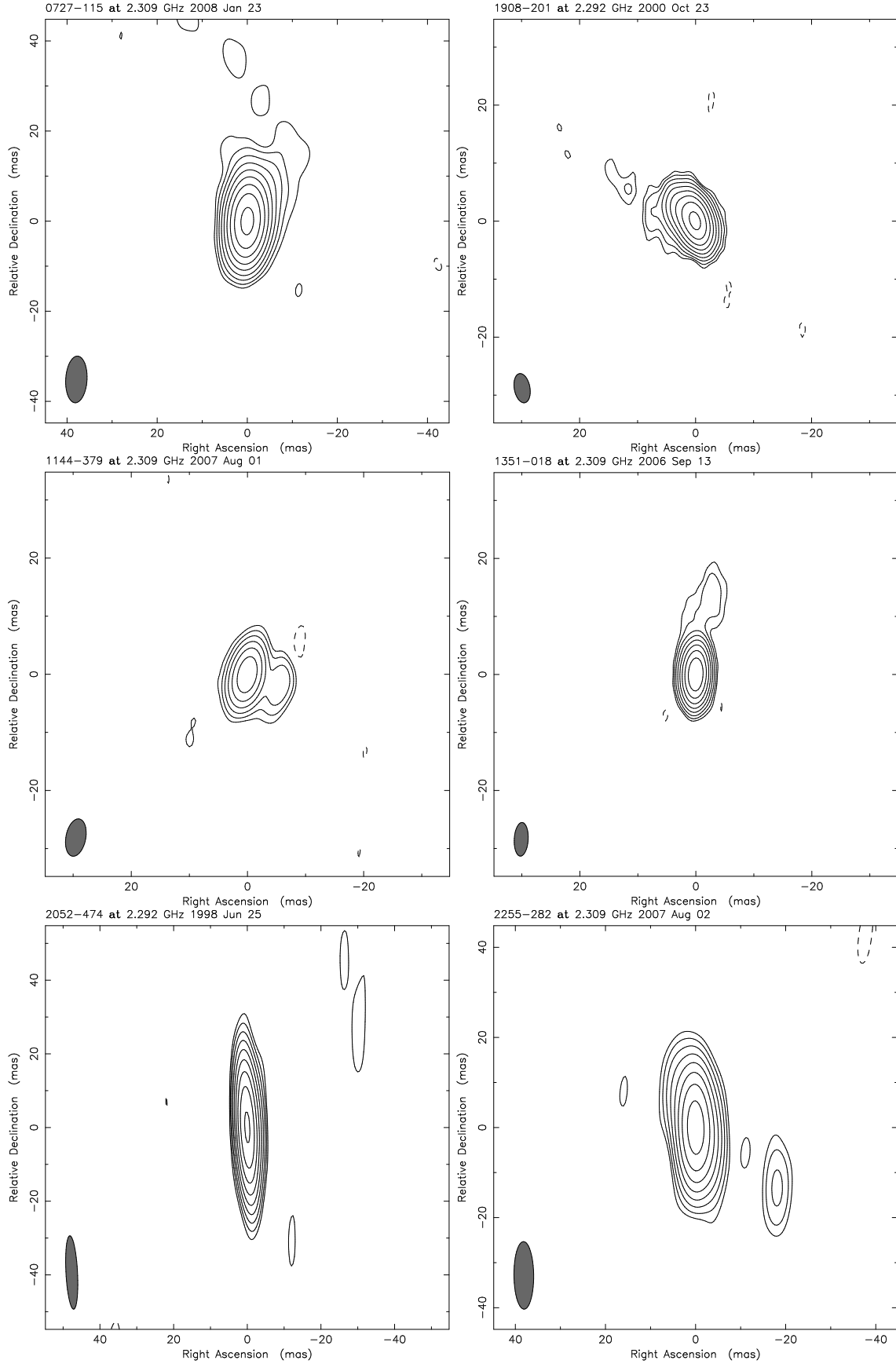


Figure 2. Two examples each of class ‘A’, ‘B’, and ‘C’ sources, respectively. Our current sample contains no examples of classes ‘D’ and ‘E’.

B1950 Source Name	Other Name	Optical ID	z	Co-ordinates		Latest Flux Densities		Latest Epoch
				RA (hh mm ss)	DEC (deg mm ss)	S_{total}	S_{core}	
0003-066	NGC1052 CTA26	BL Lac	0.35 ¹	00 06 13.89288849	-06 23 35.3353162	2.29	1.79	Jan 2008
0104-408		BL Lac	0.58 ²	01 06 45.10796851	-40 34 19.9602291	1.51	1.52	Jan 2008
0238-084		Galaxy	0.005 ³	02 41 04.79850256	-08 15 20.7517956	0.53	0.26	Dec 2007
0336-019		Quasar	0.85 ⁴	03 39 30.93778751	-01 46 35.8041062	2.53	2.16	Jan 2008
0402-362		Quasar	1.42 ⁵	04 03 53.74989835	-36 05 01.9131085	0.91	0.99	Mar 2007
0454-234		Quasar	1.00 ¹	04 57 03.17922863	-23 24 52.0201418	3.41	3.01	Dec 2007
0458-020		Quasar	2.29 ⁶	05 01 12.80988366	-01 59 14.2562534	0.82	0.65	Dec 2007
0727-115		Quasar	1.59 ⁷	07 30 19.11247420	-11 41 12.6005110	3.77	3.47	Jan 2008
0919-260		Quasar	2.30 ⁸	09 21 29.35385535	-26 18 43.3861684	1.58	1.50	Sep 2006
0920-397	3C279	Quasar	0.59 ⁹	09 22 46.41826064	-39 59 35.0683561	1.56	1.49	Jan 2008
1034-293		Quasar	0.31 ¹	10 37 16.07973476	-29 34 02.8133345	1.60	1.51	Jan 2008
1124-186		Quasar	1.05 ¹⁰	11 27 04.39244958	-18 57 17.4416582	1.16	1.16	Jan 2008
1144-379		Quasar	1.05 ¹	11 47 01.37070177	-38 12 11.0234199	1.09	1.09	Jan 2007
1145-071		Quasar	1.34 ¹¹	11 47 51.55402876	-07 24 41.1410887	0.95	0.81	Jan 2007
1253-055		Quasar	0.54 ¹²	12 56 11.16656541	-05 47 21.5247030	7.60	7.30	Dec 1998
1255-316		Quasar	1.92 ¹³	12 57 59.06081737	-31 55 16.8516980	1.51	1.38	Jan 2008
1313-333		Quasar	1.21 ¹⁴	13 16 07.98593995	-33 38 59.1725057	0.76	0.53	Feb 2004
1334-127		Quasar	0.54 ¹⁵	13 37 39.78277768	-12 57 24.6932620	2.61	2.57	Jan 2008
1351-018		Quasar	3.71 ¹⁶	13 54 06.89532213	-02 06 03.1904447	1.00	0.98	Jan 2008
1424-418		Quasar	1.52 ²	14 27 56.29756536	-42 06 19.4375991	2.04	1.66	Jan 2008
1451-375		Quasar	0.31 ¹⁷	14 54 27.40975442	-37 47 33.1448724	0.56	0.51	Jul 2006
1514-241		BL Lac	0.05 ¹⁸	15 17 41.81313221	-24 22 19.4760251	2.94	2.24	Jan 2007
1622-253		Quasar	0.79 ¹⁹	16 25 46.89164010	-25 27 38.3267989	1.01	0.99	Jan 2008
1741-038		Quasar	1.05 ²	17 43 58.85613396	-03 50 04.6166450	4.78	4.73	Jan 2008
1908-201		Quasar	1.12 ²⁰	19 11 09.65289198	-20 06 55.1089891	2.10	1.78	Dec 2007
1921-293		Quasar	0.35 ⁹	19 24 51.05595514	-29 14 30.1210524	6.18	5.43	Dec 2007
1954-388		Quasar	0.63 ²¹	19 57 59.81927470	-38 45 06.3557585	2.75	2.69	Jan 2008
1958-179	Quasar	0.65 ²¹	20 00 57.09044485	-17 48 57.6725440	1.53	1.56	Dec 2007	
2052-474	Quasar	1.49 ¹³	20 56 16.35981874	-47 14 47.6276461	1.37	1.43	Dec 2007	
2243-123	Quasar	0.63 ²¹	22 46 18.23197613	-12 06 51.2774796	2.57	1.33	Jan 2008	
2255-282	Quasar	0.93 ⁵	22 58 05.96288481	-27 58 21.2567425	0.95	0.87	Jan 2008	

Table 1. Optical and radio properties of the sample. The positions shown above are the most recent ICRF positions (Fey, Gordon & Jacobs 2009). S_{core} is the flux density in the Gaussian component fitted to the core of the latest epoch, while the total flux density S_{total} is the sum of the CLEAN components. ¹Stickel et al. (1989); ²White et al. (1988); ³Denicoló et al. (2005); ⁴Wills et al. (1978); ⁵Peterson et al. (1976); ⁶Strittmatter et al. (1974); ⁷Zensus et al. (2002); ⁸Wright et al. (1979); ⁹Hewitt & Burbidge (1989); ¹⁰Linfield et al. (1989); ¹¹Wilkes et al. (1986); ¹²Marziani et al. (1996); ¹³Jauncey et al. (1984); ¹⁴Jauncey et al. (1982); ¹⁵Stickel et al. (1993); ¹⁶Osmer et al. (1994); ¹⁷Jones et al. (2004); ¹⁸Jones et al. (2009); ¹⁹di Serego-Alighieri et al. (1994); ²⁰Halpern et al. (2003); ²¹Browne et al. (1975).

aged using Difmap in automatic mode. Generally, this mode fails for about one third of the sources which have structure that is complex or too extended for the automatic script to handle. These have to be redone by hand in interactive mode. For the southern sources in this sample, almost all had to be imaged by hand due to the poor u - v coverage.

Difmap combines the visibilities in all four 2.3 GHz receiver IFs but does not correct for spectral index effects. It was assumed that the source structure variations across the IFs were negligible (6% variation in frequency at this band). Uniform weighting was used for the initial phase self-calibration before changing to natural weighting. For our arrays, uniform weighting gives more weighting to the longer baselines whilst natural weighting gives more weighting to the shorter baselines. Images of six of the 31 sources in our sample are shown in Figure 2 with the remainder available online. Images of additional epochs can be found in the form of contour plots at the RRFID and BVID websites.

Generally, circular Gaussian models were used to fit the u - v data in order to parametrise the source morphology.

Like imaging, modelfitting is an iterative process. Elliptical Gaussian components were used only to represent the core component or a very bright jet component if the residuals remaining from a circular Gaussian model were too large and made it difficult to continue modelfitting using the residual map. The modelfits generally describe the visibility data well but these models may not be unique because of incomplete sampling in the u - v plane. In order to determine suitability of a source as a calibrator, we then determined the amount of source structure, as well as its variation with time, using several different methods based on both the CLEAN components from the Difmap imaging as well as on the parameters of the fitted Gaussians.

3 ANALYSIS AND RESULTS

Characterisation of the morphology of an AGN is very complex and no single metric is able to adequately define a good calibrator. Thus we have developed a number of complementary approaches that are described below. A weighted com-

Source Name	Epochs	Core Flux Density			Core fraction			Weighted Radial Extent			Unweighted Radial Extent		
		\bar{S}	σ_{core}	σ_{core}/\bar{S}	\bar{C}	σ_C	σ_C/\bar{C}	\bar{R}_W	σ_{R_W}	σ_{R_W}/\bar{R}_W	\bar{R}_{UW}	$\sigma_{R_{UW}}$	$\sigma_{R_{UW}}/\bar{R}_{UW}$
0003-066	24	1.55	0.31	0.20	0.64	0.07	0.11	1.67	0.40	0.24	6.17	2.22	0.36
0104-408	28	1.26	0.29	0.23	1.00	0.04	0.04	0.93	1.24	1.33	7.86	17.13	2.18
0238-084	16	0.91	0.20	0.22	0.53	0.10	0.19	0.37	0.10	0.27	17.34	16.13	0.93
0336-019	25	1.92	0.48	0.25	0.80	0.08	0.10	1.00	0.64	0.64	3.05	2.32	0.76
0402-362	17	1.22	0.11	0.09	1.00	0.03	0.03	1.18	0.26	0.22	8.11	4.54	0.56
0454-234	27	1.73	0.59	0.34	1.00	0.02	0.02	0.46	0.31	0.67	3.18	1.78	0.56
0458-020	26	0.78	0.31	0.40	0.68	0.15	0.22	2.22	1.02	0.46	16.30	17.93	1.10
0727-115	32	2.37	0.71	0.30	0.83	0.05	0.06	1.15	0.30	0.26	6.10	1.77	0.29
0919-260	17	1.32	0.83	0.63	0.73	0.11	0.15	1.70	0.34	0.20	6.46	1.55	0.24
0920-397	16	1.06	0.18	0.17	0.92	0.11	0.12	1.81	0.94	0.52	7.27	2.98	0.41
1034-293	27	1.11	0.30	0.27	0.88	0.21	0.24	0.91	0.68	0.75	5.83	8.22	1.41
1124-186	26	0.90	0.19	0.21	1.00	0.02	0.02	0.25	0.29	1.18	6.88	16.50	2.40
1144-379	23	1.34	0.39	0.29	0.83	0.05	0.06	0.44	1.79	4.10	9.61	20.66	2.15
1145-071	16	0.69	0.11	0.16	0.77	0.10	0.13	1.33	0.24	0.18	6.11	2.26	0.37
1253-055	3	6.75	0.27	0.04	0.65	0.15	0.23	2.27	0.25	0.11	12.5	0.50	0.04
1255-316	14	1.20	0.24	0.20	0.79	0.11	0.14	2.68	0.67	0.25	14.12	11.86	0.84
1313-333	17	0.80	0.28	0.35	0.71	0.05	0.07	1.29	0.40	0.31	7.82	3.05	0.39
1334-127	25	2.12	0.55	0.26	1.00	0.04	0.04	0.84	0.62	0.74	3.60	1.87	0.52
1351-018	13	0.78	0.25	0.32	1.00	0.03	0.03	1.51	2.93	1.94	2.55	1.86	0.73
1424-418	18	1.69	0.49	0.29	0.73	0.08	0.11	3.42	1.88	0.55	22.55	11.07	0.47
1451-375	14	1.11	0.30	0.27	0.88	0.07	0.08	0.37	3.71	10.08	9.31	5.40	0.58
1514-241	16	1.76	0.30	0.17	0.83	0.05	0.06	3.39	0.78	0.23	18.57	3.90	0.21
1622-253	24	1.27	0.38	0.30	0.83	0.05	0.06	1.26	0.72	0.57	6.35	7.37	1.16
1741-038	28	3.18	1.05	0.33	1.00	0.03	0.03	0.33	0.22	0.66	2.17	1.24	0.57
1908-201	23	1.95	0.45	0.23	0.77	0.07	0.09	1.50	0.45	0.30	5.60	1.68	0.30
1921-293	23	7.42	2.45	0.33	0.60	0.09	0.15	2.30	0.53	0.23	8.78	8.17	0.93
1954-388	21	2.16	0.54	0.25	1.00	0.05	0.05	0.56	0.52	0.93	3.52	2.71	0.77
1958-179	9	1.16	0.52	0.45	0.80	0.04	0.05	0.17	0.56	3.29	2.79	2.29	0.82
2052-474	10	1.36	0.34	0.25	0.81	0.29	0.36	1.33	2.09	1.56	10.45	10.66	1.02
2243-123	22	1.50	0.33	0.22	0.86	0.06	0.07	2.00	0.48	0.24	9.32	1.77	0.19
2255-282	20	0.95	1.11	1.17	0.77	0.10	0.13	2.30	2.05	0.89	6.58	3.49	0.53

Table 2. Results of variability analysis in the flux density, core fraction and radial extent.

bination of all of these metrics is eventually used to classify the suitability of each source to be a high resolution phase calibrator. These are discussed below.

3.1 Core Flux Density

A good calibrator should be relatively bright at the frequency of observation to be easily detectable. It should also be stable with minimal flux density variation over time. There is no precise definition of the AGN ‘core’ in the literature. In general the bright, compact flat spectrum feature is referred to as the core. We have confirmed our identification of the cores for our entire sample by establishing that these structures have flat or inverted spectra. This was done by using the 8.4 GHz data that are observed simultaneously with the 2.3 GHz observations presented here. Here we define a core flux density, S_{core} for each source and for each epoch as the flux density of the Gaussian component fitted to the core. The latest core flux density as defined in this section is shown, for each source in Table 1. From the core flux density, we computed the mean core flux density (\bar{S}) averaged over all epochs in which the source was observed. The extent to which the core flux density varies over time can be characterised by the core flux density variability index (σ_{core}/\bar{S}) where σ_{core} is the core flux density standard

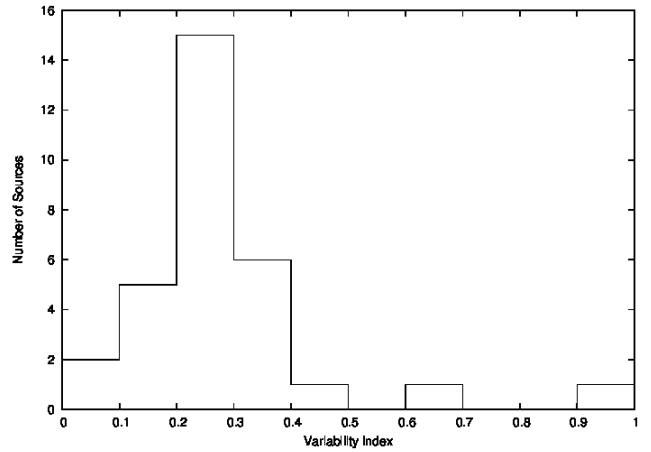


Figure 3. Distribution of the core flux density variability index.

deviation. A value of 0.0 indicates no variation over time (Table 2, column 5).

Figure 3 shows that 90 per cent of the sources have a core flux density variability index below 0.4 and 23 per cent have a variability index below 0.2 (which is below our estimated calibration uncertainties). These low variability

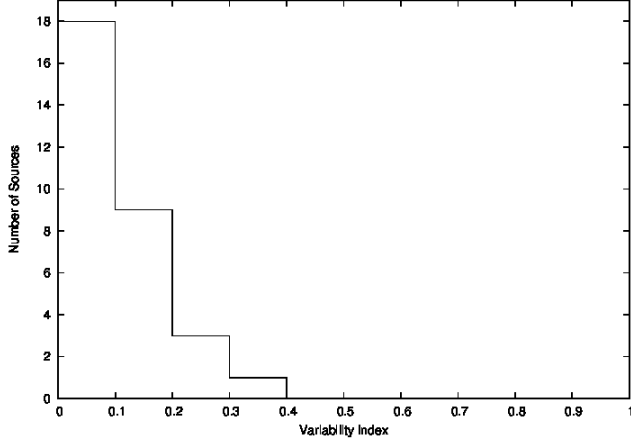


Figure 4. Distribution of the core fraction variability index. Note that all sources have an index ≤ 0.4 .

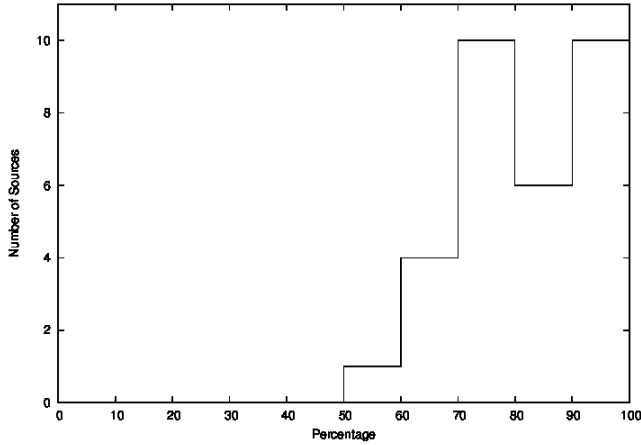


Figure 5. Distribution of the core fraction. This measure was used instead of the variability index as it shows slightly higher variation than the core fraction variability index.

indices indicate that most core fluxes in this sample are stable.

3.2 Core Fraction

Following Ojha et al. (2004b) we define a core fraction as:

$$C = S_{core_cc} / S_{total} \quad (1)$$

where S_{core_cc} is the sum of the flux densities of CLEAN components within one synthesised beam of the brightest pixel and S_{total} is the sum of all the CLEAN component flux densities.

It provides an indication of how point-like a source is and also provides a way to track source structure changes from epoch to epoch. The average core fraction, \bar{C} , was computed for each source over all epochs. As with the core flux density variability index, we also computed the source core fraction variability index (σ_C / \bar{C}) where σ_C is the core fraction standard deviation. A value of 0.0 for the source core fraction variability index indicates no variation over time. The results are shown in Table 2, column 8.

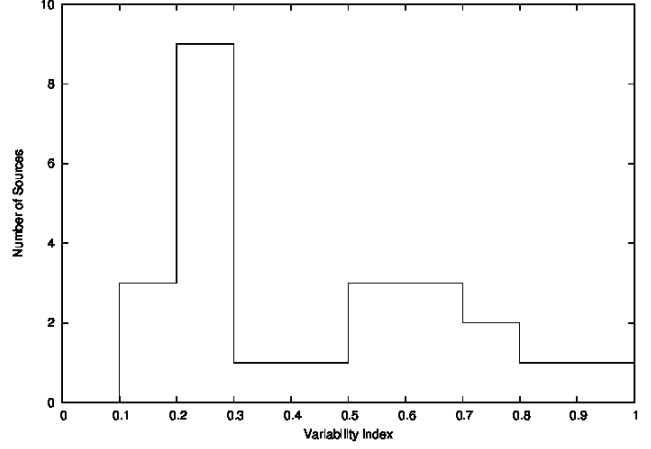


Figure 6. Distribution of the Weighted radial extent variability index. Seven sources with variability index greater than 1 are not shown in the histogram.

The distribution of the core fraction variability index is shown in Figure 4 while the distribution of the core fraction is shown in Figure 5. The mean core fraction for all the sources is 83 per cent with a standard deviation of 12 per cent. All sources have a mean core fraction variability index below 0.40. Twenty seven sources have a variability index between 0 and 0.2 and the remaining 4 between 0.21 and 0.40. In general, the southern sample sources are very compact with little variation. For this reason, we used the actual core fraction and not the variability index to classify the sources.

3.3 Flux Weighted Radial Extent

The previous two metrics are primarily measures of core-dominance. This and the following metric provide complementary information by quantifying the radial extent of the sources in the Southern sample.

The flux density weighted radial extent (Ojha et al. 2004b) is defined as:

$$R_W = \frac{\sum_i S_i r_i}{\sum_i S_i} \quad (2)$$

where R_W is in units of milliarcseconds and r_i is the radius at which the i th CLEAN component has flux density S_i .

The mean (\bar{R}_W) and standard deviation were also calculated as was the variability index (σ_{R_W} / \bar{R}_W) where σ_{R_W} is the weighted radial extent standard deviation, see Table 2, column 11.

The weighted radial extent variability index is widely distributed as shown in Figure 6, with 10 per cent of the sources having an index between 0 and 0.2, showing minimal variation in the weighted radial extent. 32 per cent of the sources have an index between 0.21 and 0.40 while 13 per cent have an index between 0.41 and 0.60. 16 per cent of the sources have an index between 0.61 and 0.80 while the rest, (29 per cent) have an index greater than 0.81. This shows a high degree of variability in the weighted radial extent.

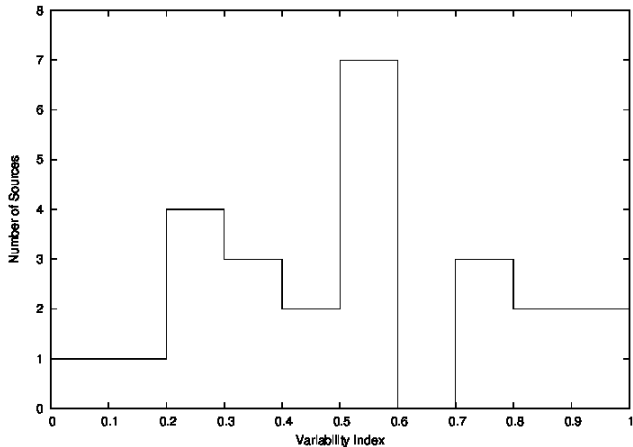


Figure 7. Distribution of the Unweighted radial extent variability index. Six sources with variability index greater than 1 are not shown in the histogram.

3.4 Unweighted Radial Extent

This is the radial extent within which 95 per cent of the source flux density is contained. This provides a measure of how extended a source is. The mean (\bar{R}_{UW}) and standard deviation were calculated as was the variability index ($\sigma_{R_{UW}}/\bar{R}_{UW}$) where $\sigma_{R_{UW}}$ is the unweighted radial extent standard deviation and R_{UW} is in units of milliarcseconds, (Table 2, column 14)

Like the weighted radial extent variability index (see above), the unweighted radial extent variability index is also widely distributed. Figure 7 shows that 6 per cent of the sources have an index below 0.2, 23 per cent have an index between 0.21 and 0.40 while 29 per cent have an index between 0.41 and 0.60. About 10 per cent have an index between 0.61 and 0.80 while 35 per cent have an index greater than 0.80, showing very high variability in the unweighted radial extent. As discussed below, this high variability (in both the weighted and unweighted radial extent) is largely a result of low brightness ‘jet’ features that are detected in some epochs but not others, usually due to differing sensitivities of the observing array rather than a real variation in the source.

4 SOURCE CLASSIFICATION

To capture the complexity of determining whether a radio source is a suitable phase calibrator for a radio interferometer, we have developed the set of complementary metrics described above. Here we discuss how we combine the information these metrics provide to arrive at a classification scheme for potential calibrators. We explain our reasons for weighting the different metrics as we have, and present our recommendations based on this weighting scheme. Since such a scheme is necessarily somewhat subjective it should be considered as reasonable and useful rather than a definitive classification.

The four metrics we used to classify the calibrator source quality were core fraction, core flux density variability index, weighted and unweighted radial extents. Each of these metrics is first assigned a score, with the scores as

Core flux density (%)	Score	Core fraction variability Index	Score
> 1	0.00		
0.91-1.00	3.5	91-100	35.0
0.81-0.90	7.0	81-90	31.5
0.71-0.80	10.5	71-80	28.0
0.61-0.70	14.0	61-70	24.5
0.51-0.60	17.5	51-60	21.0
0.41-0.50	21.0	41-50	17.5
0.31-0.40	24.5	31-40	14.0
0.21-0.30	28.0	21-30	10.5
0.11-0.20	31.5	11-20	7.0
0.01-0.10	35	1-10	3.5

Table 3. Source core fraction and core flux density variability index score distribution.

Index	Score
> 1	0.00
0.91-1.00	1.5
0.81-0.90	3.0
0.71-0.80	4.5
0.61-0.70	6.0
0.51-0.60	7.5
0.41-0.50	9.0
0.31-0.40	10.5
0.21-0.30	12.0
0.11-0.20	13.5
0.01-0.10	15

Table 4. Distribution of scores for the weighted and unweighted radial extent variability index.

shown in Tables 3 and 4. The scores for the individual metrics were chosen so as to sum to 100 for a perfect calibrator source. We also chose to score the core fraction and core flux density variability so as to give them higher weight, each having a maximum score of 35, while the two radial extents have maximum scores of 15. We use a lower maximum score for the radial extents as they are highly sensitive to small epoch-to-epoch variations in the signal-to-noise ratio of the images. Faint extended features may be detected only at some epochs depending on the signal-to-noise, resulting in a large variation in the radial-extent measures. Such low surface brightness features generally have negligible impact on the usefulness of the source as a calibrator. In any case, for a lower resolution array like MeerKAT these extended structures will be embedded in the main central component.

Based on the overall score summed up from this weighting scheme each source falls into one of five classes ‘A’ through ‘E’. A source falls into class ‘A’ if its overall score is between 80 and 100 per cent, class ‘B’ if the score is between 60 and 80 per cent, class ‘C’ if it scores between 40 and 60 per cent, class ‘D’ for any score between 20 and 40 per cent and class ‘E’ for sources scoring between 0 and 20 per cent. We propose the following classifications:

- A - Excellent calibrator (score between 80 and 100).
- B - Very good calibrator (score between 60 and 80).

Source Name	W ₁	Score W ₂	W ₃	W ₄	Total Score %	Class
0003-066	31.5	31.5	10.5	12.0	85.5	A
0104-408	28.0	35.0	0.0	0.0	63.0	B
0238-084	28.0	31.5	1.5	12.0	73.0	B
0336-019	28.0	35.0	4.5	6.0	73.5	B
0402-362	35.0	35.0	7.5	12.0	89.5	A
0454-234	24.5	35.0	7.5	6.0	73.0	B
0458-020	24.5	31.5	0.0	9.0	65.0	B
0727-115	28.0	35.0	12.0	12.0	87.0	A
0919-260	14.0	31.5	12.0	13.5	71.0	B
0920-397	31.5	31.5	9.0	7.5	79.5	B
1034-293	28.0	28.0	0.0	4.5	60.5	B
1124-186	28.0	35.0	0.0	0.0	63.0	B
1144-379	28.0	35.0	0.0	0.0	63.0	B
1145-071	31.5	31.5	10.5	13.5	87.0	A
1253-055	35.0	28.0	15.0	13.5	91.5	A
1255-316	31.5	31.5	3.0	12.0	78.0	B
1313-333	24.5	35.0	10.5	10.5	80.5	A
1334-127	28.0	35.0	7.5	4.5	75.0	B
1351-018	24.5	35.0	4.5	0.0	64.0	B
1424-418	28.0	31.5	9.0	7.5	76.0	B
1451-375	28.0	35.0	7.5	0.0	70.5	B
1514-241	31.5	35.0	12.0	12.0	90.5	A
1622-253	28.0	35.0	0.0	7.5	70.5	B
1741-038	24.5	35.0	7.5	6.0	73.0	B
1908-201	28.0	35.0	12.0	12.0	87.0	A
1921-293	24.5	31.5	1.5	12.0	69.5	B
1954-388	28.0	35.0	4.5	1.5	69.0	B
1958-179	21.0	35.0	3.0	0.0	59.0	C
2052-474	28.0	24.5	0.0	0.0	52.5	C
2243-123	28.0	35.0	13.5	12.0	88.5	A
2255-282	00.0	31.5	7.5	3.0	42.0	C

Table 5. Classification of the Sources. W₁ - Core Flux Density, W₂ - Core fraction, W₃ - Unweighted Radial Extent, W₄ - Weighted Radial Extent

- C - Good calibrator (score between 40 and 60).
D - Use with caution (score between 20 and 40).
E - Unsuitable as calibrator (score below 20).

In our sample (Table 5), we have 9 class ‘A’ sources, 19 class ‘B’ sources and 3 class ‘C’ sources. There are no sources in class ‘D’ and class ‘E’. Thus all the sources in our sample would be ‘Good’ calibrators and all but three sources are likely to be ‘Very Good’ calibrators.

5 CONCLUSIONS

We modelfitted up to 32 epochs of observations (average of 20 epochs) for each of the 31 sources in our sample which was selected from the RRFID Kinematic Survey (Piner et al. 2007) and determined their suitability as phase calibrators. While the kinematic survey looks more at proper motion in the sources at 8.4 GHz, this paper concentrates on the morphological properties of the sources at 2.3 GHz, a frequency more relevant to emerging southern hemisphere arrays like MeerKAT and ASKAP.

We have developed a method to classify radio sources according to their suitability as phase calibrators for radio interferometers. We first characterize a source by calculating

several metrics which give measures of the degree to which the core dominates the source, and the degree of variability, both in flux density, and the degree to which the source is extended. These metrics are then combined to give the source a total score, which is used to assign the source to one of five classes of suitability as a calibrator. All 31 sources in our sample were classified as ‘Good’ calibrators with 28 classified as ‘Very good’ or better.

ACKNOWLEDGMENTS

FH is supported by a grant from the South African SKA project and HartRAO. FH thanks the United States Naval Observatory for their hospitality during two visits in 2008 and 2010. This research has made use of the United States Naval Observatory (USNO) Radio Reference Frame Image Database (RRFID) and Laboratoire d’Astrophysique de Bordeaux (LAB) Bordeaux VLBI Image Database (BVID). This research has made use of NASA’s Astrophysics Data System Bibliographic Services and the NASA/IPAC Extragalactic Database (NED) which is operated by the Jet Propulsion Laboratory, California Institute of Technology, under contract with the National Aeronautics and Space Administration.

REFERENCES

- Booth R.S., de Block W.J.G., Jonas J.L. and Fanaroff B., 2009, ArXiv e-prints, 0910.2935
Browne I.W.A., Savage A. and Bolton J.G., 1975, MNRAS, 173, 87P
Carilli C.L. and Rawlings S., 2004, New Astronomy Review, 48, 979
Collioud A. and Charlot P., 2009, 19th European VLBI for Geodesy and Astrometry Working Meeting, 19
Denicoló G., Terlevich R., Forbes D.A., Terlevich A. and Carrasco L., 2005, MNRAS, 356, 1440
di Serego-Alighieri S., Danziger I.J., Morghanti R., and Tadhunter C.N., 1994, MNRAS, 269, 998
Fey A.L. and Charlot P., 1997, ApJS., 111, 95
Fey A.L. and Charlot P., 2000, ApJS., 128, 17
Fey A.L., Clegg A.W. and Fomalont E.B., 1996, ApJS., 105, 299
Fey A.L. et al., 2004, AJ., 127, 1791
Fey A.L., Ojha R., Reynolds J.E., Ellingsen S.P., McCulloch P.M., Jauncey D.L. and Johnston K.J., 2004, AJ., 128, 2593
Fey A.L. et al., 2006, AJ., 132, 1994
Fey A.L., Gordon D. and Jacobs S., 2009., IERS Technical Note 35, ISBN 3-89888-918-6, 204
Greisen E.W., 1998, Astronomical Society of the Pacific Conference Series, 145, 204
Halpern J.P., Eracleous M. and Mattox J.R., 2003, AJ, 125, 572
Hewitt A. and Burbidge G., 1989, A new catalog of quasi-stellar objects
Jauncey D.L., Batty M.J., Gulkis S. and Savage A., 1982, AJ, 87, 763
Jauncey D.L., Batty M.J., Wright A.E., Peterson B.A., and Savage A., 1984, ApJ, 286, 498

- Jones D.H. et al., 2004, The 6dF Galaxy Survey Data Release 1
- Jones D.H. et al., 2009, The 6dF Galaxy Survey Data Release 3
- Johnston S. et al., 2008, *Experimental Astronomy*, 22, 151
- Linfield R.P. et al., 1989, *ApJ*, 336, 1105
- Ma C. et al., 1998, *AJ*, 116, 516
- Marziani P., Sulentic J.W., Dultzin-Hacyan D., Calvani M., and Moles M., 1996, *ApJS*, 104, 37
- Ojha R. et al., 2004, *AJ*, 127, 3609
- Ojha R., Fey A.L., Jauncey D.L., Lovell J.E., Johnston K.J., 2004, *ApJ*, 614, 607
- Ojha R. et al., 2005, *AJ*, 130, 2529
- Osmer P.S., Porter A.C. and Green R.F., 1994, *ApJ*, 436, 678
- Peterson B.A., Jauncey D.L., Condon J.J., and Wright A.E., 1976, *ApJ*, 207, L5
- Piner B.G., Mahmud M., Fey A.L. and Gospodinova K., 2007, *AJ*, 133, 2357
- Rees M.J., 1997, *Reviews in Modern Astronomy*, 10, 179
- Schilizzi, R. T. et al., 2007, *SKA Memo*, 100
- Shepherd M.C., Pearson T.J. and Taylor G.B., 1995, *BAAS*, 27, 903
- Stickel M., Fried J.W. and Kuehr H., 1989, *A&AS*, 80, 103
- Stickel M., Kuehr H. and Fried J.W., 1993, *A&AS*, 97, 483
- Strittmatter P.A., Carswell R.F., Gilbert G., and Burbidge E.M., 1974, *ApJ*, 190, 509
- Veron-Cetty M.P., Veron P., 2003, *Astron. Astrophys.*, 412, 399
- White G.L., Jauncey D.L., Wright A.E., Batty M.J., Savage A., Peterson B.A., Gulkis S., 1988, *ApJ*, 327, 561
- Wilkes B.J., 1986, *MNRAS*, 218, 331w
- Wills D., and Lynds R., 1978, *ApJS*, 36, 317
- Wright A.E., Peterson B.A., Jauncey D.L., and Condon J.J., *ApJ*, 229, 73
- Zensus J.A., Ros E., Kellerman K.I., Cohen M.H., Vermeulen R.C., and Kadler M., 2002, *AJ*, 124, 662

This paper has been typeset from a \LaTeX file prepared by the author.